Airborne Ultrasound Detection via Refractive Index Modulation of Air Using Sagnac Interferometry

Zijian Wang [ID], Yosuke Mizuno [ID], *Senior Member, IEEE*, and Kentaro Nakamura [ID], *Member, IEEE*

Abstract—**Airborne ultrasound is increasingly recognized as a crucial technology for short-range sonar applications in vehicles and drones, as well as for the development of haptic devices, noncontact manipulation of small objects, medical imaging, and material evaluation. This paper presents a novel approach using a fiber-based Sagnac interferometer to detect acoustically induced modulations of the air's refractive index with a minimal setup. This method offers immunity to low-frequency thermal fluctuations and vibratory disturbances while circumventing the complexities and expenses associated with optical components. By eliminating mechanical moving parts, the system benefits from enhanced robustness and operates without the need for recalibration. Initially, a theoretical analysis of the operating principle is provided, followed by experimental validation, which demonstrates the capability to measure ultrasound frequencies ranging from 26.4 to 96.1 kHz using fiber delay coils spanning 100 to 1000 m. Techniques for assessing sound pressure levels are also discussed. Furthermore, the integration of an electro-optic modulator into the system is discussed, highlighting its significant contributions to improving the system's responsivity, linear dynamic range, and stability.**

Index Terms—**Airborne, refractive index, Sagnac interferometer, ultrasound.**

I. INTRODUCTION

AIRBORNE ultrasound is an essential technology for proximity sensing of vehicles and drones [1]. At the same time, high-intensity airborne ultrasound is attracting attention as a method for haptic devices [2], noncontact manipulation of small objects [3], medical imaging [4], as well as structural health monitoring (SHM), and non-destructive testing (NDT) in civil and mechanical structures [5]. Traditional methods of using microphones for airborne ultrasound measurements have several shortcomings, primarily stemming from their membrane structure. These issues encompass limited frequency response due to mechanical resonance, susceptibility to electromagnetic signal interference, nonlinearities under high sound pressure, the need for frequent calibration, and high costs associated with large-area multi-channel measurements.

Quantitative instrumentation of ultrasonic sound pressure is emerging as the key technology for developing novel airborne ultrasonic methods. Numerous optical ultrasonic sensors, known for their high sensitivity and wide frequency response, have been extensively developed for ultrasound detection and imaging. Additionally, owing to their distributed sensing potential, a wide range of sensing materials, and high flexibility in bending, they are widely employed in non-contact ultrasound detection, proving particularly attractive in scenarios involving high temperatures and intricate contours where traditional detection methods face challenges. [6]

The primary directions in optical ultrasonic sensors include optical resonant cavity acoustic sensors, fiber Bragg grating (FBG) acoustic sensors, and optical fiber interferometric acoustic sensors. Optical resonant cavity acoustic sensors have garnered significant attention due to their exceptionally high sensitivity and array potential [7], [8]. In 2023, YANG et al. successfully fabricated a microdisk resonant cavity sensor with a peak sensitivity of $1.18 \ \mu Pa \ Hz^{-1/2}$ at 82.6 kHz [9].

FBG acoustic sensors offer shorter measurement lengths, superior spectral characteristics, and greater ease of multiplexing compared to optical fiber interferometric sensors. However, they exhibit lower sensitivity and shifts in the spectrum of the sensing FBG due to large variations in quasi-static measurands can lead to changes in the sensitivity of the detection system. Research on FBG acoustic sensors for ultrasonic measurements began with Webb et al. in 1996 [10]. Subsequently, various system configurations of FBG acoustic sensors have been proposed for ultrasonic detection [11], [12] and photoacoustic imaging [13], [14].

Optical fiber interferometric acoustic sensors are based on various interference principles: Michelson interferometer, Mach-Zehnder interferometer, Fabry-Perot interferometer, Sagnac interferometer, as well as polarization interferometer, and mode interferometer. Compared to optical resonant cavity acoustic sensors, optical fiber interferometric acoustic sensors have lower manufacturing complexity and costs. In contrast to FBG acoustic sensors, optical fiber interferometric acoustic sensors exhibit higher sensitivity. Furthermore, compared to the other two types of acoustic sensors, optical fiber interferometric acoustic sensors also offer advantages in terms of system and device consistency, enhanced signal-to-noise ratio, and calibration reliability [15]. In 1977, Bucaro et al. first reported the use of a fiber-optic Mach-Zehnder interferometer for acoustic wave detection [16]. Subsequently, fiber-optic Mach-Zehnder interferometers

[17], [18], [19] and other configurations such as Michelson interferometers [20], [21], [22], Sagnac interferometers [23], [24], [25], [26], [27], [28], [29], Fabry-Perot interferometers (FPI) [30], [31], [32], [33], [34] and polarization interferometers [35] have also been developed for ultrasonic detection.

Several studies have explored the detection of sound or ultrasound using fiber-optic interferometers [36], [37], [38], [21], where the vibration of the fiber or diaphragm translates sound pressure into variations in optical path length. However, relying on mechanical vibrations limits the frequency response due to the mechanical resonance. To circumvent the limitations posed by mechanical components, alternative strategies have been developed. Among these, the employment of a fiber-optic probe based on reflectivity changes [36], [39], [40] has shown promise. On the other hand, interferometric techniques that measure the modulation of air's refractive index caused by sound pressure have attracted attention from various groups [41], [42], [43] because of their superior sensitivity over the fiber-optic reflectivity approach. Nonetheless, these interferometric systems often grapple with sensitivity to external perturbations such as vibration, alongside their complexity and high cost. In contrast, the Sagnac interferometer presents clear advantages over these methods. As a path-matching device, it exhibits immunity to low-frequency thermal fluctuations and vibration disturbances.

In this work, we introduce a fiber-based Sagnac interferometer modified by substituting one side of the Sagnac fiber loop with an air gap. This modification permits light to travel through the air for a certain distance, enabling the detection of acoustically induced refractive index modulation of air. Building upon our preliminary findings shared at a conference [44], this study introduces enhancements to the experimental setup, including the use of a fiber circulator to improve component immunity to disturbances and ensure the symmetry of the Sagnac coil. To further advance system performance, an electro-optic modulator (EOM) is incorporated to generate a high-frequency carrier, establishing stable orthogonal phase bias working points. This configuration not only ensures high responsivity, and a wide linear dynamic range but also enhances system stability by shifting the sensor signal to a higher frequency spectrum, thereby simplifying signal processing and amplification. Our approach effectively eliminates the necessity for mechanical movements, heralding a new era of broader frequency range detection with calibration-free features.

II. ULTRASOUND DETECTION VIA AIR REFRACTIVE INDEX MODULATION: PRINCIPLES

A. Sound Pressure-Induced Refractive Index Changes of Air

First, let us summarize the relationship between the sound pressure and the resultant change in the refractive index of the air [45], [46]. We assume that the change rate of the volume of air $\Delta V/V$ is equal to that of the optical refractive index of the air $\Delta n/(n_a - 1)$:

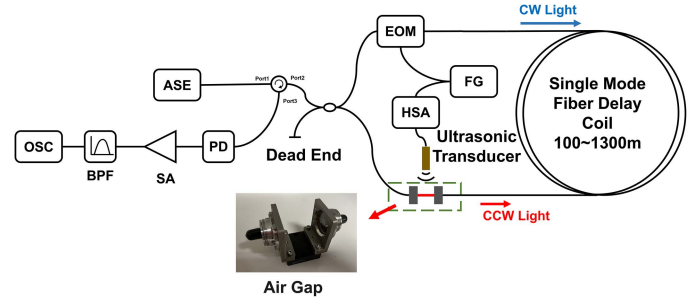$$\frac{\Delta V}{V} = -\frac{\Delta n}{n_a - 1}. \tag{1}$$

Fig. 1. Sound pressure detection using fiber-optic Sagnac interferometer with the air gap. OSC, oscilloscope; BPF, bandpass filter; SA, signal amplifier; PD, photodetector; ASE, amplified spontaneous emission; EOM, electro-optic modulator, FG, function generator; HSA, high-speed amplifier.

The adiabatic condition can be applied to ultrasonic waves, and

$$PV^\gamma = (P + p)(V + \Delta V)^\gamma = \text{const.}, \tag{2}$$

where p and P represent the sound pressure and atmospheric pressure, respectively. γ is the ratio of the specific heat of air $(= 1.4)$, and ρ is the density of air. Under the condition that the acoustic changes are much smaller than the static volume and pressure, we have

$$\frac{\Delta V}{V} = -\frac{p}{\gamma P}. \tag{3}$$

The sound speed of air is given as

$$c = \sqrt{\frac{\gamma P}{\rho}}. \tag{4}$$

From (1)–(4), the variation in the refractive index is given as a function of the sound pressure:

$$\Delta n = \frac{n_a - 1}{c^2 \rho} p = 1.93 \times 10^{-9} p = \alpha p. \tag{5}$$

Here, α $(= 1.93 \times 10^{-9} \text{Pa}^{-1})$ is the sensitivity constant.

B. System Configuration Overview

A basic fiber-optic Sagnac interferometer shown in Fig. 1 is used in this study. A series of fiber coils made of a standard single-mode fiber (length of 100 m, 200 m, 1000 m, compatible with SMF-28) are combined to the length of 100 to 700 m (interval 100 m), 1000 m, 1300 m, and then connected to a light source and a photodetector. An amplified spontaneous emission (ASE) light source (ASE-FL7004, 1530-1610 nm, FIBERLABS) and an integrated photo receiver (2053-FC-M, NEWPORT) were used in the experiments. The ASE light source and optical receiver are connected to the same port of the 2x2 fiber coupler (TW1550R5F2, 1550 ± 100 nm, 50:50 Split, FC/PC, THORLABS) through a fiber circulator, this port is a reciprocity port, the two beams of light interfering at this port will only undergo coupling once when passing through the fiber coupler, and the interfering signals output from this port will not be affected by the coupling phase shift of the fiber coupler. A significant stability improvement of the fiber coupler was observed in the experiments.

Two fiber ports (PAF2A-7C, FC/APC, $F = 7.5$ mm, THOR-LABS) were used to create an air gap of 7.5~45 mm, which is introduced in one end of the fiber coil and works as an acoustically sensitive part. Angled cuts were applied to the air gap to minimize the reflection. Difficulty in spatial adjustment caused a transmission loss of around 5.4 dB across the air gap. An electro-optic modulator (EOM, LNP6118, THORLABS) was used to provide a high-frequency carrier. Since only the input port of the EOM used a polarization-maintaining (PM) fiber, a section of the PM fiber is connected at its output port in the experiments to ensure the consistency of the modulation to clockwise (CW) and counter-clockwise (CCW) lights by the EOM. Significant stability improvement of the EOM modulation was observed.

A 1/8-inch condenser microphone (Type 7118, ACO) was used to verify the characteristics of the sensing system.

C. Sagnac Ultrasonic Sensor With Air Gap

Phase modulation in the air gap due to sound pressure φ is

$$\varphi = \frac{2\pi\Delta n}{\lambda}g, \tag{6}$$

where λ and g are the wavelength of light and the gap distance, respectively. If the sound pressure is sinusoidal at the angular frequency of ω_a,

$$p = p_0 \cos\omega_a t. \tag{7}$$

From (5)–(7), the phase modulations at the photodetector surface for the CW and CCW lights are

$$\varphi_{CW} = \frac{2\pi\alpha p_0}{\lambda}g\cos\omega_a t, \tag{8}$$

and

$$\varphi_{CCW} = \frac{2\pi\alpha p_0}{\lambda}g\cos\omega_a\left(t - \frac{n_f L}{v}\right), \tag{9}$$

respectively, where n_f, v, and L are the refractive index of the fiber core, the speed of light in vacuum, and the length of the fiber coil, respectively. The sensing air gap is assumed to be located at the input side for the CCW light. Electric fields of the CW and CCW lights are expressed as

$$E_1 = E_{CW} \times e^{-i(\varphi_{CW})}, \tag{10}$$

and

$$E_2 = E_{CCW} \times e^{-i(\varphi_{CCW}+\theta)}, \tag{11}$$

respectively. Here, θ is the initial phase difference intrinsic to the Sagnac loop, which is zero in the ideal case. The photocurrent of the photodiode is

$$i \propto E_{CW}{}^2 + E_{CCW}{}^2$$
$$+ 2E_{CW}E_{CCW}\cos\left(\varphi_{CW} - \varphi_{CCW} - \theta\right). \tag{12}$$

The phase modulation difference due to ultrasound for the CW and CCW lights $\varphi_{CW} - \varphi_{CCW}$ can be written as

$$\theta_a = \frac{4\pi\alpha p_0}{\lambda}g\sin\left(\omega_a t\right)\sin\frac{\omega_a n_f L}{2v}. \tag{13}$$
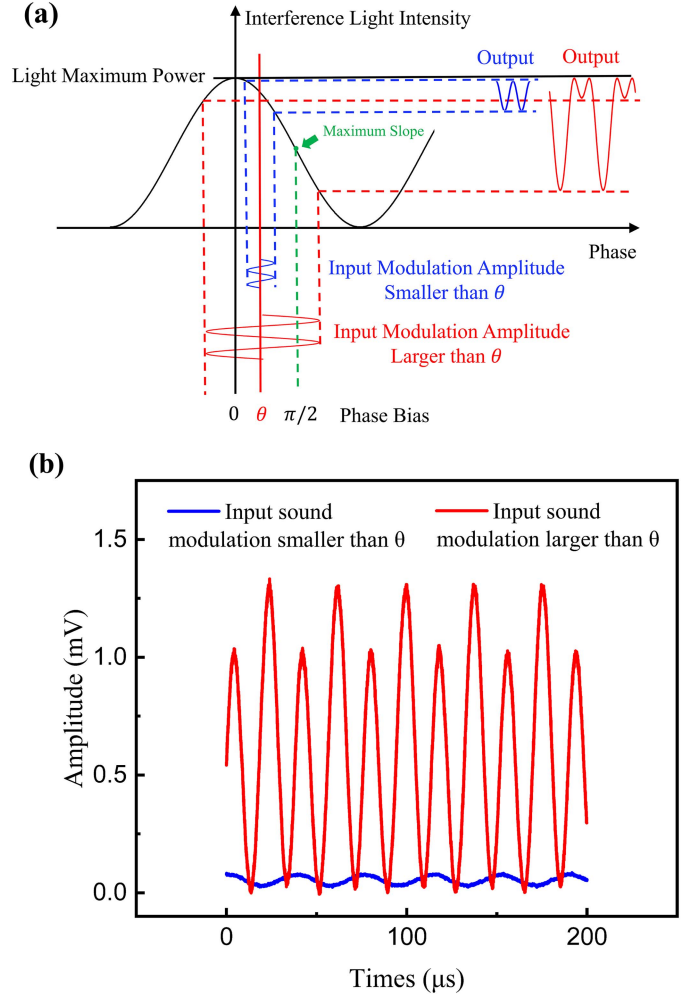

Fig. 2. Typical sensor responses. (a) Relation between input modulation amplitude and output and (b) temporal variations of the output signal: blue, the maximum value of θ_a is smaller than θ; red, the maximum value of θ_a is larger than θ.

Then, (12) can be rewritten as

$$i \propto E_{CW}{}^2 + E_{CCW}{}^2 + 2E_{CW}E_{CCW}\cos\left(\theta_a - \theta\right). \tag{14}$$

Fig. 2(a) and (b) show the optical interference caused by the ultrasonic modulation and thus the output intensity change. When the maximum value of θ_a is smaller than θ, the output voltage waveform is almost sinusoidal at the same frequency as the applied ultrasonic field. In the case that the maximum value of θ_a is higher than θ, output voltage waveform is folded, and the major frequency component is doubled. Two peaks exhibit different amplitudes since the initial phase difference is not ideal.

From the above results, we understand that the sensitivity to sound pressure is determined by the factor $\sin\frac{\omega_a n_f L}{2v}$, and it shows the maximum for

$$L = \frac{v}{2n_f f_a}. \tag{15}$$

Here, f_a is the ultrasonic frequency. Considering that v and n_f are the speed of light and the fiber core refractive index, respectively, a fiber coil of 1 km is required to obtain the
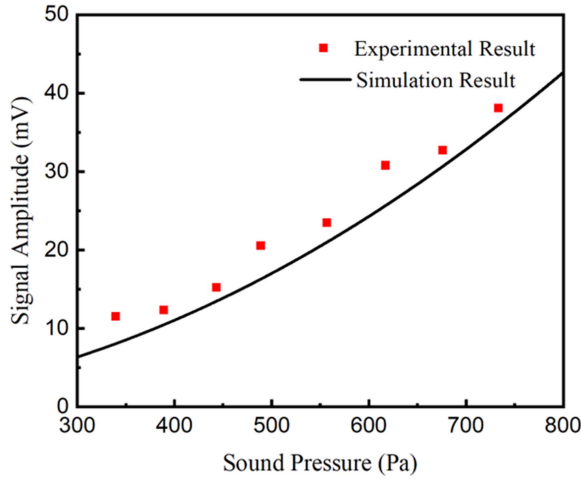
Fig. 3. The relationship between sound pressure and sensor signal amplitude.

Fig. 4. The relationship between fiber coil length and sensor signal amplitude.

maximum sensitivity at the ultrasonic frequency of 100 kHz. Ultrasonic sensitivity is reduced as the frequency is lowered. This nature of the Sagnac interferometer provides robustness to low-frequency external disturbance.

III. UNMODULATED MEASUREMENT RESULTS

A. Correlation Between Sensor Signal Amplitude and Sound Pressure

A duralumin stepped horn connected to a bolt-clamped Langevin transducer was driven at its fundamental frequency of 26.4 kHz. The output surface of the horn of 30 mm in diameter was located near the air gap of the Sagnac fiber coil, and the sound pressure applied to the air gap was 10∼800 Pa (114∼152 dB), variation in the refractive index of air caused by sound pressure is about $1.93 \times 10^{-8} \sim 1.54 \times 10^{-6}$, which can be calculated by (5)). Fig. 3 summarizes the photodetector output voltage as a function of the sound pressure. The output AC voltage increased with increasing sound pressure p, as expected by $\alpha p[1 - \cos(\frac{\omega_a n_f L}{2v})]$.

B. Impact of Fiber Coil Length on Output Voltage

A 26.4 kHz transducer was used to verify the effect of the Sagnac coil length on the system responsivity. Fig. 4 summarizes the photodetector output voltage as a function of the length of the fiber coil. The output AC voltage increased as the fiber coil length L, as expected by $1 - \cos(\sin \frac{\omega_a n_f L}{2v})$, and the matching coil length for the 26.4 kHz ultrasound is calculated to be 3792 m. Fig. 5 shows the output voltage waveform for the sound pressure level of 111 dB, which was the minimum detectable level in this experiment.

C. Frequency Response Analysis

Subsequently, frequency responses of the proposed sensor were evaluated using another Langevin transducer connected to a rectangular duralumin stepped horn with a radiation surface of 10 mm in length and 5 mm in width. The fundamental resonance
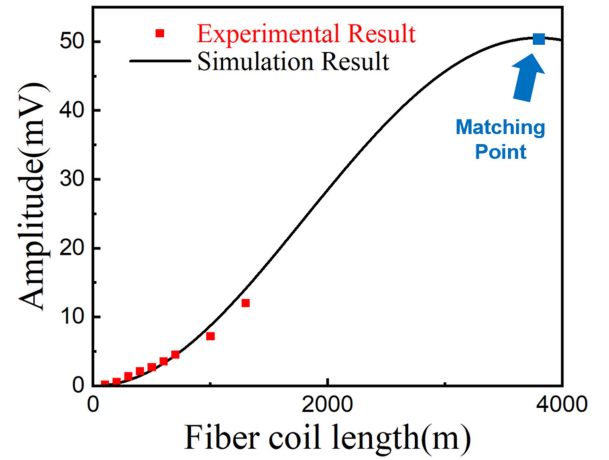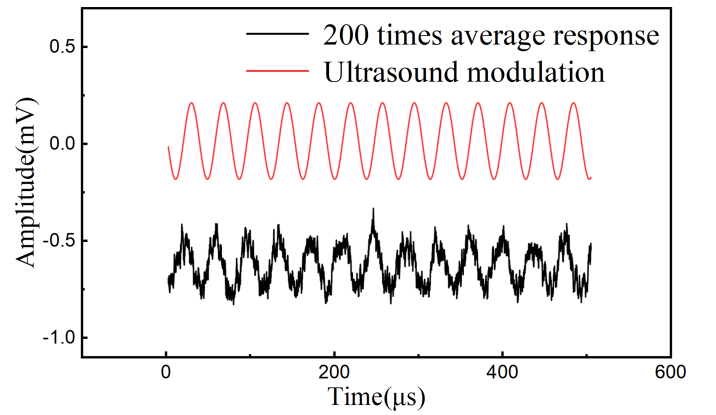

Fig. 5. Output average waveform for the sound pressure level of 111 dB.

and higher overtones of the transducer system at around 28.6, 56.8, 79.0, and 96.1 kHz were utilized. To keep the sound pressure the same for different operating frequencies of the sound source, we adjusted the driving current of the transducer and monitored the sound pressure with a calibrated instrumental 1/8-inch condenser microphone.

An EOM was inserted into the other end of the Sagnac coil to compare the results with the refractive index modulation of air due to airborne ultrasound. Fig. 6 shows the results with phase modulation by the EOM. Here, the length of the Sagnac coil was 1 km. The output signals exhibited the maximum at around the expected frequency.

The discrepancies between experimental results and theoretical predictions in ultrasonic measurements can be attributed to the complex distribution of sound fields over gap lengths. This complexity arises because the experiments were conducted under near-field conditions on the radiating surface of the transducer. Consequently, influences such as transducer output sidelobes, ultrasonic diffraction between gap interfaces, and reflection issues are present. However, the experimental results of the EOM modulation contrast are found to be closer to simulated results that incorporate intrinsic phase shift.
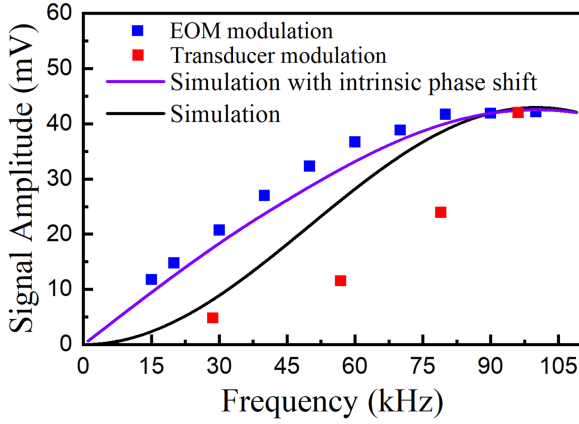
Fig. 6. Frequency response of the proposed sensing systems compared with the modulation by an EOM.
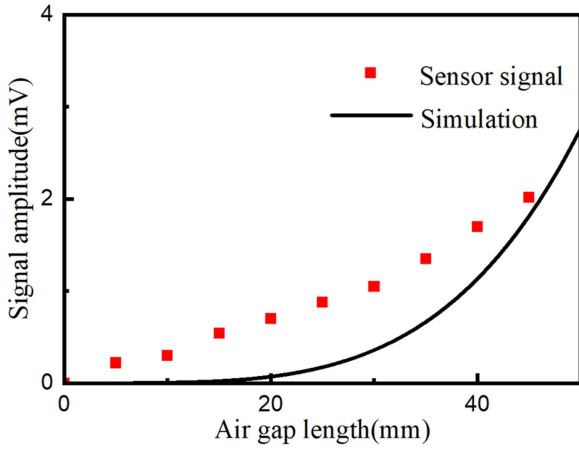

Fig. 7. Sensor signal amplitude result of effective sensing light path sweep.
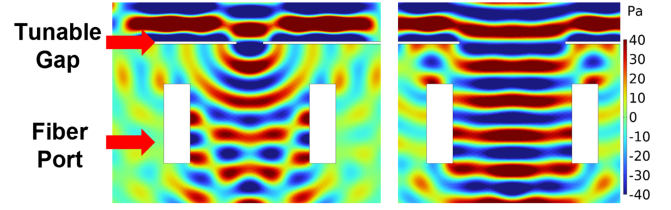

Fig. 8. Air gap sound field distribution under 5 mm width (left) and 40 mm width (right) tunable gap.
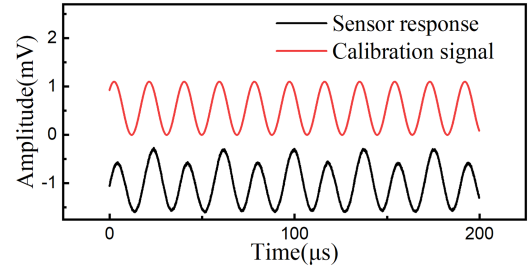
Fig. 9. Experimental sensor response signal with the maximum value of θ_a over than θ.

D. Influence of Air Gap Length on Measurements

We placed a tunable gap (tunable range $0 \sim 45$ mm, adjustment step 5 mm.) between the air gap and the sound source to adjust the width of the sound field entering the air gap. Affected by the size of the fiber port, the distance between the tunable gap and the light propagating in the air gap is about 15 mm. The output AC voltage increased as the air gap length l increased, as expected by the expression of sound pressure: $l \times [1 - \cos(\frac{\omega_a n_f L}{2v})]$. The results are summarized in Fig. 7.

The discrepancy between the observed experimental outcomes and theoretical predictions, as elaborated in III. C may stem from the intricate ultrasonic field distribution across the air gap. This complexity and discrepancy may originate from the diffraction by the tunable gap and ultrasonic reflections within the air gap. The acoustic fields at the air gap with tunable gap at 10 mm and 40 mm are given in Fig. 8, which clearly shows the effect of the gap size on the acoustic field distribution, and the system response matches the theoretical results to a progressively higher degree with the increase in the tunable gap.

E. Exploring Initial Intrinsic Phase Shift Effects

Voltage waveforms at the photodetector output in the previous experiments were almost sinusoidal shape at the frequency of applied ultrasonic fields as long as the ultrasonic sound pressure was sufficiently low. This means that the experimental setup has an initial finite phase difference between the CW and CCW lights: $\theta \neq 0$. The measured signal shall be affected by the magnitude of the initial phase difference θ.

We can estimate the initial phase difference of the system from the output waveforms and estimated modulation due to ultrasound for a moderately high sound pressure as follows. Fig. 9 is a typical case, where the ultrasonic frequency is 26.4 kHz (the period is 37.92 μs). As can be seen from the figure, the output signal waveform (black curve) is folded, and the fundamental frequency is doubled. The peaks are up and down alternatively if we see the waveform carefully. The calibration signal was created with the use of the EOM which can give a known phase modulation. By analyzing the difference between adjacent peaks, we can estimate the initial phase difference θ. After some calculations, we obtained that the initial phase difference intrinsic to the experimental setup was $\theta = 0.32°$ (at this point, the optical path length difference between the CW and CCW directions, caused by nonlinear effects, is approximately 2.76 nm), where $\theta_a = 3.75°$ for the ultrasonic sound pressure level of 150.9 dB.

F. Fiber Coupler Reciprocity Port Stability Effect

The use of reciprocal ports has dramatically improved the stability of fiber coupler, as elaborated in II.B, In the experiment, we simultaneously test the output of the fiber coupler from the reciprocal port led by the circulator (the port of ASE input) and the non-reciprocal port (the dead end in Fig. 1) and observe the stability of the output signal amplitude of the two ports by applying external vibration to the fiber coupler, the results are shown in Fig. 10. The output signal from reciprocal port led by the circulator shows excellent stability to the perturbation. The non-reciprocal port, due to a relatively
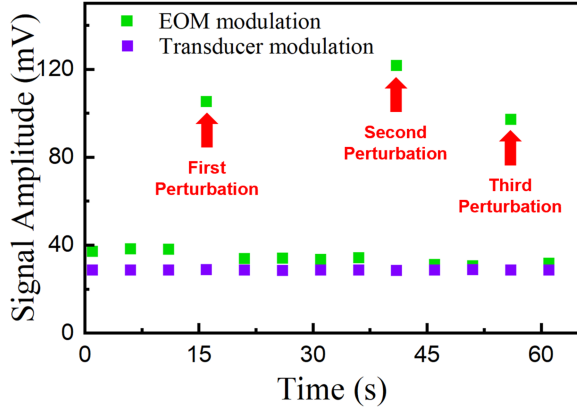
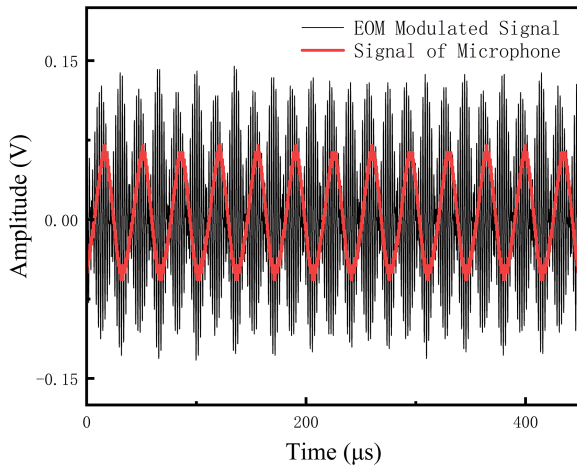Fig. 10.   EOM modulated signal and microphone signal.

Fig. 11.   EOM modulated signal and microphone signal.

Fig. 12.   The relationship between sound pressure and sensor signal amplitude.

Fig. 13.   Spectrum of the EOM modulated signal.

large initial phase difference, has an amplitude slightly greater than the reciprocal port signal but is very sensitive to the perturbation.

IV. MODULATED MEASUREMENT RESULTS

While the Sagnac system exhibits characteristics of insensitivity to low-frequency disturbances, the use of non-polarization-maintaining optical fibers renders the inherent phase difference in the system susceptible to external perturbations, thereby affecting the path-matching properties of the Sagnac system. To address this issue, determining the optimal orthogonal phase difference between the CW and CCW optical paths holds the potential to significantly enhance the system's stability. Moreover, this approach may lead to increased responsivity and a broader linear response dynamic range.

We employed an EOM to provide the system with a phase modulation at a frequency of 500 kHz, generating a high-frequency carrier signal with an amplitude range of $\pm90°$. The envelope of the carrier signal establishes an orthogonal working point for the system, concurrently shifting the frequency of the sensing signal to a more suitable high-frequency range for amplification. The results are summarized in Fig. 11 .
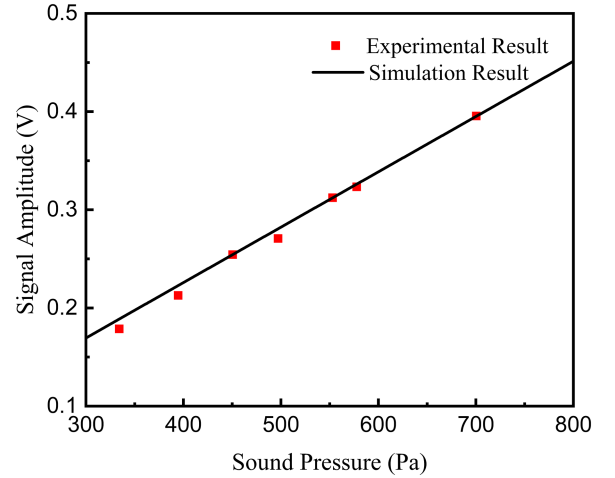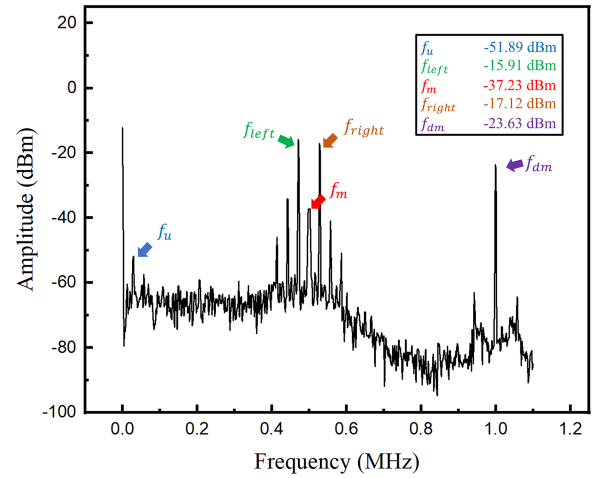
The same Langevin transducer was driven at its fundamental frequency at 26 kHz. The output surface of the horn of 30 mm in diameter was located near the air gap of the Sagnac fiber coil, and the sound pressure applied to the air gap was $10\sim800$ Pa. Fig. 12 summarizes the photodetector output voltage as a function of the sound pressure. The output AC voltage increased as the sound pressure p, as expected by $\alpha p \times \sin(\frac{\omega_a n_f L}{2v})$. Compared to Fig. 3, the sensor modulated using the EOM demonstrates significantly better linearity, responsivity, and stability.

As illustrated in Fig. 13, the received signal exhibits clear results of double-sideband modulation, including five major components: the ultrasonic signal at frequency f_s =28.6 kHz, the carrier signal at frequency f_m =499.6 kHz, the double-sideband signals at frequencies $f_{left} = f_m - f_s$ =471.2 kHz and $f_{right} = f_m + f_s$ =528.1 kHz, and the carrier harmonic signal at frequency f_{dm} =999.2 kHz. Notably, the sideband component at frequency f_{left} and f_{right} is amplified by 35.98 dB and 42.77 dB compared to the original signal, significantly enhancing the system's sensitivity and anti-interference capabilities.

V. CONCLUSION

We explored the measurement of airborne ultrasonic pressure using a streamlined Sagnac interferometer setup, which consists of a fiber-optic loop coil with an air gap introduced at one end of the loop. Sound pressure was accurately measured by observing the phase modulation caused by changes in the refractive index at the air gap. We conducted experimental investigations on the intrinsic phase difference within the Sagnac loop and applied this knowledge to reconstruct the ultrasound signal. A high-frequency carrier signal was introduced to the system using an EOM, fine-tuning the amplitude of this carrier signal to be near the quadrature working point. This technique allowed for the optimal phase difference between the CW and CCW paths in the loop, markedly increasing the sensor's sensitivity, expanding the linear response dynamic range, and enhancing its resistance to disturbances.

This approach proved to be highly effective for the detection of ultrasound signals at higher frequencies and sound pressures. It was observed that certain characteristics of the sensor, such as its bandwidth and dynamic range, could be tailored by adjusting structural parameters including the length of the air gap and the fiber coil. However, due to the complexity of operating in higher modes and the near-field characteristics of the sound source, some uncertainty in the absolute sound pressure sensitivity was noted. To lessen the impact of the sensing area on the acoustic field, future work could focus on minimizing the gap coupler's size or rethinking the gap's design.

REFERENCES

[1] M. Kunita, "Range measurement in ultrasound FMCW system," *Electron. Commun. Jpn.*, vol. 90, pp. 9–19, 2007.

[2] T. Hoshi, M. Takahashi, T. Iwamoto, and H. Shinoda, "Noncontact tactile display based on radiation pressure of airborne ultrasound," *IEEE Trans. Haptics*, vol. 3, no. 3, pp. 155–165, Jul.–Sep. 2010.

[3] R. Nakamura, Y. Mizuno, and K. Nakamura, "Demonstration of noncontact ultrasonic mixing of droplets," *Jpn. J. Appl. Phys.*, vol. 52, no. 7, 2013, Art. no. 07HE02.

[4] D. Dalecki et al., "Advancing ultrasound technologies for tissue engineering," in *Handbook of Ultrasonics and Sonochemistry*. Singapore: Springer, 2016, pp. 1101–1126.

[5] E. Blomme, D. Bulcaen, and F. Declercq, "Air-coupled ultrasonic NDE: Experiments in the frequency range 750 kHz–2 MHz," *NDT E Int.*, vol. 35, no. 7:pp. 417–426, 2022.

[6] X. Bao, "Prospects on ultrasound measurement techniques with optical fibers," *Meas. Sci. Technol.*, vol. 34, no. 5, 2023, Art. no. 051001.

[7] H. Fan et al., "Ultrasound sensing based on an in-fiber dual-cavity Fabry–Perot interferometer," *Opt. Lett.*, vol. 44, no. 15, pp. 3606–3609, 2019.

[8] X. Ma et al., "Fiber optic-based laser interferometry array for three-dimensional ultrasound sensing," *Opt. Lett.*, vol. 44, no. 23, pp. 5852–5855, 2019.

[9] H. Yang et al., "Micropascal-sensitivity ultrasound sensors based on optical microcavities," *Photon. Res.*, vol. 11, pp. 1139–1147, 2023.

[10] D. J. Webb et al., "Miniature fiber optic ultrasonic probe," *Proc. SPIE*, vol. 2839, pp. 76–80, 1996.

[11] B. Culshaw, G. Thursby, D. Betz, and B. Sorazu, "The detection of ultrasound using fiber-optic sensors," *IEEE Sensors J.*, vol. 8, no. 7, pp. 1360–1367, Jul. 2008.

[12] C. Broadway et al., "A compact polymer optical fibre ultrasound detector," *Photons Plus Ultrasound: Imag. Sens.*, 2016, vol. 9708, 2016.

[13] Y. Liang et al., "Fiber-laser-based ultrasound sensor for photoacoustic imaging," *Sci. Rep.*, vol. 7, no. 1, 2017, Art. no. 40849.

[14] Y. Liang et al., "Optical-resolution functional gastrointestinal photoacoustic endoscopy based on optical heterodyne detection of ultrasound," *Nature Commun.*, vol. 13, no. 1, 2022, Art. no. 7604.

[15] G. Wild and S. Hinckley, "Acousto-ultrasonic optical fiber sensors: Overview and state-of-the-art," *IEEE Sensors J.*, vol. 8, pp. 1184–1193, Jul. 2008.

[16] J. A. Bucaro, H. D. Dardy, and E. F. Carome, "Optical fiber acoustic sensor," *Appl. Opt.*, vol. 16, no. 7, pp. 1761–1762, 1977.

[17] D. Gallego and H. Lamela, "High sensitivity interferometric polymer optical fiber ultrasound sensors for optoacoustic imaging and biomedical application," *Proc. SPIE*, vol. 7753, pp. 1039–1042, 2011.

[18] M. H. Chen et al., "A novel fiber optic interferometer of hydrophone based on Mach-Zehnder hybrid configuration," *Proc. SPIE*, vol. 6189, pp. 527–537, 2006.

[19] H. Wen et al., "High-sensitivity fiber-optic ultrasound sensors for medical imaging applications," *Ultrason. Imag.*, vol. 20, no. 2, pp. 103–112, 1988.

[20] C. Sun and F. Ansari, "Design of the fiber optic distributed acoustic sensor based on Michelson interferometer and its location application," *Opt. Eng.*, vol. 42, pp. 2987–2993, 2003.

[21] L. Liu et al., "Fiber-optic Michelson interferometric acoustic sensor based on a PP/PET diaphragm," *IEEE Sensors J.*, vol. 16, no. 9, pp. 3054–3058, May 2016.

[22] X. L. Zhang, Z. Meng, and Z. L. Hu, "Sensing system with Michelson-type fiber optical interferometer based on single FBG reflector," *Chin. Opt. Lett.*, vol. 9, no. 11, pp. 73–75, 2011.

[23] P. A. Fomitchov, S. Krishnaswamy, and J. D. Achenbach, "Compact phase-shifted Sagnac interferometer for ultrasound detection," *Opt. Laser Technol.*, vol. 29, no. 6, pp. 333–338, 1997.

[24] P. A. Fomitchov et al., "Intrinsic fiber optic Sagnac ultrasound sensor for process monitoring in composite structures," *Proc. SPIE*, vol. 3589, pp. 156–159, 1999.

[25] P. A. Fomitchov et al., "Extrinsic and intrinsic fiberoptic Sagnac ultrasound sensors," *Opt. Eng.*, vol. 39, no. 7, pp. 1972–1984, 2000.

[26] P. A. Fomitchov, A. K. Kromine, S. Krishnaswamy, and J. D. Achenbach, "Sagnac-type fiber-optic array sensor for detection of bulk ultrasonic waves," *IEEE Trans. Ultrasonics, Ferroelectr., Freq. Control*, vol. 47, no. 3, pp. 584–590, May 2000.

[27] T. S. Jang et al., "Surface-bonded fiber optic Sagnac sensors for ultrasound detection," *Ultrasonics*, vol. 42, no. 1–9, pp. 837–841, 2004.

[28] M. A. Churgin, M. Liu, and T. Buma, "Fiber optic Sagnac interferometer for characterizing ultrasound biomicroscopy transducers," in *Proc. IEEE Int. Ultrasonics Symp.*, 2009, pp. 952–955.

[29] Y. Wang et al., "Partial discharge ultrasound detection using the Sagnac interferometer system," *Sensors*, vol. 18, no. 5, 2018, Art. no. 1425.

[30] J. J. Alcoz, C. E. Lee, and H. F. Taylor, "Embedded fiber-optic Fabry-Perot ultrasound sensor," *IEEE Trans. Ultrason. Ferroelectr. Freq. Control*, vol. 37, no. 4, pp. 302–306, Jul. 1990.

[31] J. F. Dorighi, S. Krishnaswamy, and J. D. Achenbach, "Stabilization of an embedded fiber optic Fabry-Perot sensor for ultrasound detection," *IEEE Trans. Ultrasonics, Ferroelectr., Freq. Control*, vol. 42, no. 5, pp. 820–824, Sep. 1995.

[32] P. C. Beard and T. N. Mills, "Extrinsic optical-fiber ultrasound sensor using a thin polymer film as a low-finesse Fabry–Perot interferometer," *Appl. Opt.*, vol. 35, no. 4, pp. 663–675, 1996.

[33] P. C. Beard and T. N. Mills, "Miniature optical fibre ultrasonic hydrophone using a Fabry-Perot polymer film interferometer," *Electron. Lett.*, vol. 33, no. 9, pp. 801–803, 1997.

[34] J. Ma, H. Xuan, H. L. Ho, W. Jin, Y. Yang, and S. Fan, "Fiber-optic Fabry-Perot acoustic sensor with multilayer graphene diaphragm," *IEEE Photon. Technol. Lett.*, vol. 25, no. 10, pp. 932–935, May 2013.

[35] S. C. Rashleigh, "Acoustic sensing with a single coiled monomode fiber," *Opt. Lett.*, vol. 5, no. 9, pp. 392–394, 1980.

[36] H. Takei, T. Hasegawa, K. Nakamura, and S. Ueha, "Measurement of intense ultrasound field in air using fiber optic probe," *Jpn. J. Appl. Phys.*, vol. 46, no. 7S, pp. 4555–4558, 2007.

[37] K. Nakamura, *Ultrasonic Transducers*. Sawston, U.K.: Woodhead Publishing, 2012.

[38] K. Nakamura, M. Hirayama, and S. Ueha, "Measurements of air-borne ultrasound by detecting the modulation in optical refractive index of air," in *Proc. IEEE Ultrason. Symp. Proc.*, 2002, pp. 609–612.

[39] B. Shen et al., "Fiber-optic ultrasonic probe based on refractive-index modulation in water," *Proc. SPIE*, vol. 7753, pp. 1454–1457, May 2011.

[40] J. M. S. Sakamoto et al., "High sensitivity fiber optic angular displacement sensor and its application for detection of ultrasound," *Appl. Opt.*, vol. 51, no. 2, pp. 4841–4851, 2012.

[41] Y. Ikeda et al., "Observation of traveling wave with laser tomography," *Acoustical Sci. Technol.*, vol. 37, pp. 231–238, 2016.

[42] E. Udd, "Fiber-optic acoustic sensor based on the Sagnac interferometer," *Proc. SPIE*, vol. 425, pp. 90–95, 1983.

[43] S. Knudsen and K. Blotekjar, "An ultrasonic fiber-optic hydrophone incorporating a push-pull transducer in a Sagnac interferometer," *J. Lightw. Tech.*, vol. 12, no. 9, pp. 1696–1700, Sep. 1994.

[44] Z. Wang et al., "Detection of airborne ultrasound through modulation of refractive index of air using Sagnac interferometer," presented at the 28th International Conference on Optical Fiber Sensors, Hamamatsu, Japan, Nov. 2023, Paper Th6. 50.

[45] T. S. Jang and S. S. Lee, "Noncontact detection of ultrasonic waves," *IEEE Trans. Ultrasonics, Ferroelectr., Freq. Control*, vol. 49, no. 6, pp. 767–775, 2002.

[46] K. Nakamura, *Ultrasonics: Physics and Applications*. Bristol, U.K.: IOP Publishing, 2022.

Zijian Wang received the B.E. degree in opto-electronics information science and engineering from Zhejiang University, Hangzhou, China, in 2019, and the M.E. degree in electrical and electronic engineering in 2023 from the Tokyo Institute of Technology, Yokohama, Japan, where he is currently working toward the Dr.Eng. degree in optical acoustic sensing.

Yosuke Mizuno (Senior Member, IEEE) received the B.E., M.E., and Dr. Eng. degrees in electronic engineering from The University of Tokyo, Tokyo, Japan, in 2005, 2007, and 2010, respectively. From 2010 to 2012, he was a Research Fellow (PD) with the Japan Society for the Promotion of Science, and he worked on polymer optics with the Tokyo Institute of Technology, Tokyo. In 2011, he was a Visiting Research Associate with the BAM Federal Institute for Materials Research and Testing, Berlin, Germany. From 2012 to 2020, he was an Assistant Professor with the Tokyo Institute of Technology. Since 2020, he has been an Associate Professor with the Faculty of Engineering, Yokohama National University, Yokohama, Japan, where he is active in fiber-optic sensing and polymer optics. Prof. Mizuno is a member of the Japanese Society of Applied Physics, the Optical Society of Japan, and the Institute of Electronics, Information, and Communication Engineers of Japan. He was the recipient of the Funai Information Technology Award in 2017, Optics Design Award in 2018, and Young Scientist's Award in 2021, Commendation for Science and Technology, Minister of Education, Culture, Sports, Science and Technology.

Kentaro Nakamura (Member, IEEE) received the B.E., M.E., and Dr.Eng. degrees from the Tokyo Institute of Technology, Yokohama, Japan, in 1987, 1989, and 1992, respectively. Since 2010, he has been a Professor with the Precision and Intelligence Laboratory (currently, Institute of Innovative Research), Tokyo Institute of Technology, Tokyo, Japan. His research interests include the applications of ultrasonic waves, measurement of vibration and sound using optical methods, and fiber-optic sensing. Prof. Nakamura is a member of the Acoustical Society of Japan, Japan Society of Applied Physics (JSAP), Institute of Electronics, Information and Communication Engineers, and Institute of Electrical Engineers of Japan. He was the recipient of the Awaya Kiyoshi Award for Encouragement of Research from ASJ in 1996, and Best Paper Awards from IEICE in 1998 and from the Symposium on Ultrasonic Electronics in 2007 and 2011. He was also the recipient of the Japanese Journal of Applied Physics Editorial Contribution Award from JSAP in 2007.